

Article

# Ultrasonic-Assisted Electrodeposition of Mn-Doped NiCo<sub>2</sub>O<sub>4</sub> for Enhanced Photodegradation of Methyl Red, Hydrogen Production, and Supercapacitor Applications

Kuan-Ching Lee <sup>1</sup>, Timm Joyce Tiong <sup>1,\*</sup>, Guan-Ting Pan <sup>2</sup> , Thomas Chung-Kuang Yang <sup>3</sup> , Kasimayan Uma <sup>4</sup>, Zong-Liang Tseng <sup>4</sup> , Aleksandar N. Nikoloski <sup>2,\*</sup>  and Chao-Ming Huang <sup>5,\*</sup> 

<sup>1</sup> Department of Chemical and Environmental Engineering, University of Nottingham, Broga Road, Semenyih 43500, Selangor Darul Ehsan, Malaysia

<sup>2</sup> College of Science, Health, Engineering & Education, Murdoch University, 90 South Street, Murdoch, WA 6150, Australia; kuan-ting.pan@murdoch.edu.au

<sup>3</sup> Department of Chemical Engineering and Biotechnology, National Taipei University of Technology, Taipei 10608, Taiwan; ckyang@mail.ntut.edu.tw

<sup>4</sup> Organic Electronics Research Center, Ming Chi University of Technology, New Taipei City 24301, Taiwan; umamahesh16@gmail.com (K.U.); zltseng@mail.mcut.edu.tw (Z.-L.T.)

<sup>5</sup> Green Energy Technology Research Center, Department of Advanced Applied Materials Engineering, Kun Shan University, No. 195, Kunda Rd., Yongkang Dist., Tainan 710303, Taiwan

\* Correspondence: joyce.tiong@nottingham.edu.my (T.J.T.); a.nikoloski@murdoch.edu.au (A.N.N.); charming@mail.ksu.edu.tw (C.-M.H.)

**Abstract:** This paper presents a novel ultrasonic-assisted electrodeposition process of Mn-doped NiCo<sub>2</sub>O<sub>4</sub> onto a commercial nickel foam in a neutral electroplating bath (pH = 7.0) under an ultrasonic power of 1.2 V and 100 W. Different sample properties were studied based on their crystallinity through X-ray diffraction (XRD), morphology was studied through scanning electron microscopy (SEM), and photodegradation was studied through ultraviolet–visible (UV–Vis) spectrophotometry. Based on the XRD results, the dominant crystallite phase obtained was shown to be a pure single NiCo<sub>2</sub>O<sub>4</sub> phase. The optical properties of the photocatalytic film showed a range of energy band gaps between 1.72 and 1.73 eV from the absorption spectrum. The surface hydroxyl groups on the catalytic surface of the Mn-doped NiCo<sub>2</sub>O<sub>4</sub> thin films showed significant improvements in removing methyl red via photodegradation, achieving 88% degradation in 60 min, which was approximately 1.6 times higher than that of pure NiCo<sub>2</sub>O<sub>4</sub> thin films. The maximum hydrogen rate of the composite films under 100 mW/cm<sup>2</sup> illumination was 38 μmol/cm<sup>2</sup> with a +3.5 V external potential. The electrochemical performance test also showed a high capacity retention rate (96% after 5000 charge–discharge cycles), high capacity (260 Fg<sup>−1</sup>), and low intrinsic resistance (0.8 Ω). This work concludes that the Mn-doped NiCo<sub>2</sub>O<sub>4</sub> hybrid with oxygen-poor conditions (oxygen vacancies) is a promising composite electrode candidate for methyl red removal, hydrogen evolution, and high-performance hybrid supercapacitor applications.

**Keywords:** ultrasonic; electrodeposition; NiCo<sub>2</sub>O<sub>4</sub>; photodegradation; hydrogen production; supercapacitor



**Citation:** Lee, K.-C.; Tiong, T.J.; Pan, G.-T.; Yang, T.C.-K.; Uma, K.; Tseng, Z.-L.; Nikoloski, A.N.; Huang, C.-M. Ultrasonic-Assisted Electrodeposition of Mn-Doped NiCo<sub>2</sub>O<sub>4</sub> for Enhanced Photodegradation of Methyl Red, Hydrogen Production, and Supercapacitor Applications. *J. Compos. Sci.* **2024**, *8*, 164. <https://doi.org/10.3390/jcs8050164>

Academic Editor: Francesco Tornabene

Received: 27 February 2024

Revised: 17 April 2024

Accepted: 23 April 2024

Published: 29 April 2024



**Copyright:** © 2024 by the authors. Licensee MDPI, Basel, Switzerland. This article is an open access article distributed under the terms and conditions of the Creative Commons Attribution (CC BY) license (<https://creativecommons.org/licenses/by/4.0/>).

## 1. Introduction

Semiconductor photocatalysts have been widely studied and used in the treatment of environmental pollution owing to their ability to produce hydrogen and oxygen from water. Titanium dioxide (TiO<sub>2</sub>) is among the most used semiconductor photocatalysts due to its high efficiency of 13% [1,2]. However, titanium dioxide has a large 3.2 eV band gap energy, reducing its efficiency under visible light. Therefore, many studies have attempted to improve TiO<sub>2</sub> photocatalyst activity under visible light, including through oxygen deficiency generation [3,4] and metal doping [5,6]. As a result of these

efforts, despite the light absorption of  $\text{TiO}_2$  having been increased to the visible light region [7], its thermal instability or carrier recombination centers increasingly affect these processes [8–11]. However, improvements are still required if  $\text{TiO}_2$  is to be used as a photocatalyst, causing researchers to venture into other materials for use within the visible light region.

Recently, Cui et al. [12] found transition metal oxide  $\text{NiCo}_2\text{O}_4$  nanoplatelets to be novel and promising photocatalysts for methyl blue degradation due to their small particle size (80–150 nm) and excellent optical properties (band gap between 2.06 and 3.63 eV). Wan et al. [13] performed an investigation on  $\text{NiCo}_2\text{O}_4$  catalyst preparation for the degradation of methyl red under visible light irradiation, and they found that the methyl red photodegradation efficiency of mesoporous  $\text{NiCo}_2\text{O}_4$  can reach 95.1% under visible light irradiation for 2 h. Additionally, the demonstrated effectiveness of  $\text{NiCo}_2\text{O}_4$  in photodegradation within the visible region has enhanced the popularity of this mixed oxide compound, mainly due to its multiple valence states, hypotonicity, ultrastability, and containable structure [12]. To further enhance the properties of  $\text{NiCo}_2\text{O}_4$ , one typical method that has gained popularity over recent years is performing transition metal doping onto a semiconductor film [14,15]. Han et al. [16] synthesized Cu-doped  $\text{NiCo}_2\text{O}_4$  nanosheets using a thermal method for energy storage applications. The electrochemical properties of the Cu– $\text{NiCo}_2\text{O}_4$  electrode can be improved due to its high conductivity and effective mass transfer. Additionally, it is worth noting that the electrochemical properties of  $\text{NiCo}_2\text{O}_4$  can also be enhanced by Al doping due to the transportation of electrons/ions and the large specific surface area for redox reactions in the reaction system [14]. In the context of Mn doped onto  $\text{NiCo}_2\text{O}_4$ , there have been several recent reports on the enhancement that Mn provides in their respective domains. Nguyen et al. [17] successfully doped Mn onto  $\text{NiCo}_2\text{O}_4$  using hydrothermal methods followed by a subsequent calcination route. They showed significant increments in the power density of their supercapacitor. Similar results were obtained by Pradeepa et al. [18], in which Mn-doped  $\text{NiCo}_2\text{O}_4$  improved the specific capacitance, electrode stability, and transfer speed of charge carriers. Liang et al. [19] found that spinel Mn– $\text{NiCo}_2\text{O}_4$  can effectively shorten the transmission path of Li ions, thereby improving the overall conductivity of Li-ion batteries.

Research on preparing binder-free composite electrodes using nickel as the base material has aroused great interest in recent years [7,20–23]. Binder-free electrodes enhance the contact between the active electrode material and the current collector, significantly reducing the risk of catalyst shedding during cycling and improving cycle stability [7]. Among the synthesis methods for binder-free electrodes, electrodeposition synthesis offers a wide range of benefits due to its improved catalyst uniformity, providing consistent grain sizes across the catalytic surface [24]. One common approach to enhancing the electrodeposition technique is to employ ultrasound during the synthesis process to improve the anti-corrosivity [25], magnetitic intensity [26], degree of wear [27], and hardness [28] properties of composite films. Researchers have reported several ultrasonic-assisted synthesis methods. For example, Costa et al. [29] found that using ultrasound for catalyst preparation improved their catalyst's surface chemical group properties. Additionally, Shi et al. [30] reported that the introduction of ultrasonic-assisted electrodeposition can improve the particle's surface distribution and impede catalyst aggregation on the substrate. The ultrasonic-assisted electrodeposition approach can provide a benefit in that hydrogen bubbles and film oxides are removed, leading to porosity in thin films and improvements in their electrode efficiency in systems [31]. Despite the emerging popularity of  $\text{NiCo}_2\text{O}_4$  and the increased use of Mn as a dopant to improve overall catalytic activity, there are still no records on electrodeposition synthesis using ultrasound for ternary metal oxide catalyst preparation from a precursor mixture.

In this work, we report a facile combined ultrasonic-assisted electrodeposition method for preparing Mn-doped NiCo<sub>2</sub>O<sub>4</sub> composite electrodes to investigate the effects of different molar ratios of Ni/Co/Mn on the characteristics of catalysts, such as their morphology, crystallinity, and functional groups. The resulting Mn-doped NiCo<sub>2</sub>O<sub>4</sub> composite electrodes show high potential for environmental protection through methyl red removal, energy utility in hydrogen evolution, and energy storage.

## 2. Materials and Methods

### 2.1. Materials

The precursors of Ni<sup>2+</sup>, Co<sup>2+</sup>, and Mn<sup>2+</sup> ions for the reaction of Mn/Ni/Co/O thin films were analytical-grade nickel(II) nitrate hexahydrate (Ni(NO<sub>3</sub>)<sub>2</sub>•6H<sub>2</sub>O), cobalt(II) nitrate hexahydrate (Co(NO<sub>3</sub>)<sub>2</sub>•6H<sub>2</sub>O), and manganese(II) nitrate hydrate (Mn(NO<sub>3</sub>)<sub>2</sub>•H<sub>2</sub>O) with purities of >99%, all of which were purchased from Merck. The commercial nickel foam substrates (2 × 3 cm) were acquired from Sigma-Aldrich Co (Taipei City, Taiwan). Before the deposition process, the commercial nickel foam substrates were cleaned in different baths of acetone, deionized (DI) water, and ethyl alcohol using an ultrasonic cleaning machine for 30 min in each bath. The nickel foam substrates were then blown dry with nitrogen gas.

### 2.2. Preparation of Mn-Doped NiCo<sub>2</sub>O<sub>4</sub> Electrodes

Mn-doped NiCo<sub>2</sub>O<sub>4</sub> thin films were prepared on the commercial nickel foam substrates via ultrasonic-assisted electrochemical deposition. The solution (250 mL) of electrochemical deposition was made of aqua solutions of Mn(NO<sub>3</sub>)<sub>2</sub>•H<sub>2</sub>O (0.04M), Co(NO<sub>3</sub>)<sub>2</sub>•6H<sub>2</sub>O (0.04 M), Na<sub>2</sub>SO<sub>4</sub> (0.04 M), and Ni(NO<sub>3</sub>)<sub>2</sub>•6H<sub>2</sub>O (0.04 M). All of the samples were prepared with varying molar ratios of Ni/Co/Mn, as summarized in Table 1. All thin films were deposited using a galvanostat (Autolab Model PGSTAT 30, Herisau, Switzerland) with a standard three-electrode system (the commercial nickel foam, a 4 × 10 cm<sup>2</sup> platinum sheet, and a saturated calomel electrode were respectively used as a working electrode, a counter electrode, and reference electrodes) connected to an electrochemical Pyrex glass cell. Figure 1 shows the setup of the ultrasonic-assisted electrochemical deposition of the Mn-doped NiCo<sub>2</sub>O<sub>4</sub> electrodes. Deposition voltage and time were set at 1.2 V and 15 min for all samples. During the electrodeposition process, an additional ultrasonic power of 100 W (Qsonica, Q700, 20 kHz, Newtown, CT, USA) was employed for the ultrasonicated samples. After deposition, dark brown films were deposited on the nickel foam substrates (working electrodes) in the three-electrode electrodeposition system. After this, all of the samples were annealed in a furnace at 500 °C for 60 min following a stable ramping rate (5 °C/min) from 30 °C. The temperature was then gradually cooled down to an ambient temperature (25 °C) in an air atmosphere.

**Table 1.** Summary of synthesis parameters in the reaction.

Samples	Mole Ratios of Ni:Co:Mn	pH Value	Ultrasound Power (W)	Annealed Temperature (°C)
A(u)	1:1:0.0	7	-	500
B(u)	1:1:0.2	7	-	500
C(u)	1:1:0.4	7	-	500
D(u)	1:1:0.6	7	-	500
E(u)	1:1:0.8	7	-	500
F(u)	1:1:1.0	7	-	500
A(s)	1:1:0.0	7	100	500
B(s)	1:1:0.2	7	100	500
C(s)	1:1:0.4	7	100	500
D(s)	1:1:0.6	7	100	500
E(s)	1:1:0.8	7	100	500
F(s)	1:1:1.0	7	100	500

(u) un-sonicated; (s) sonicated.

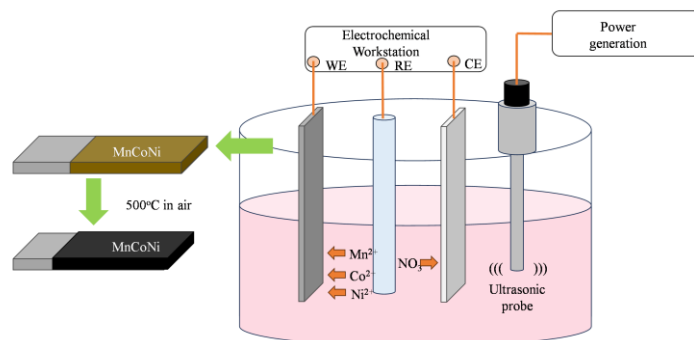


**Figure 1.** Deposition method of Mn-doped  $\text{NiCo}_2\text{O}_4$  electrodes.

### 2.3. Characterization of the Mn-Doped $\text{NiCo}_2\text{O}_4$ Electrodes

Crystalline patterns of all of the samples were obtained using X-ray diffraction (Rigaku RINT 2000, TX, USA) with  $\text{Cu K}\alpha$  radiation ( $\lambda = 1.5405 \text{ \AA}$ ) in a  $2\theta$  scan range of  $10^\circ$  to  $80^\circ$ . The spectral absorbance of all of the samples was measured using ultraviolet-visible (UV-Vis) spectrophotometry (PerkinElmer Lambda 900, Shelton, CT, USA) with a wavelength range from 500 to 1100 nm at ambient temperature. The thin film morphology in this study was analyzed using a field emission scanning electron microscope (JEOL JSM 6700F, Peabody, MA, USA) with energy-dispersive X-ray analysis (OXFORD X-MaxN, accelerating voltage, 15.0 kV, High Wycombe, UK). The textural properties of the samples were obtained via the Barrett–Emmett–Teller approach using a Micromeritics Instrument Corporation device (TriStar II Plus, Norcross, GA, USA).

### 2.4. Photocatalytic Performance Evaluation of the Mn-Doped $\text{NiCo}_2\text{O}_4$ Electrodes

Photocatalytic performance was evaluated via photodegradation of the methyl red solution under visible irradiation using the Mn-doped  $\text{NiCo}_2\text{O}_4$  electrodes. Before the visible radiation evaluation, the methyl red aqueous solution (60 mL, 10 ppm) was stirred using a magnetic stirrer (CORNING, 200 rpm, New York, NY, USA) for adsorption analysis under dark surroundings for 30 min. Visible irradiations were acquired using a 500 W xenon lamp equipped with cut-off filters to eliminate wavelengths of light lower than 420 nm. The methyl red concentration in the solution was analyzed using ultraviolet-visible spectrophotometry at 30 min intervals for 150 min.

### 2.5. Electrochemical Measurements

Half-cell electrochemical measurements of different molar ratios of Ni/Co/Mn for the Mn-doped  $\text{NiCo}_2\text{O}_4$  electrodes were performed in a 6 M KOH electrolyte. For the half-cell measurements, active electrode material/Ni foam was used as the working electrode, saturated calomel electrode (SCE) as the reference electrode, and platinum plate as the counter electrode. Cyclic voltammetry (CV) analyses were recorded from 100 to 5  $\text{mVs}^{-1}$ . Galvanostatic charge and discharge (GCD) analyses were recorded from 10 to 1  $\text{Ag}^{-1}$ . Electrochemical impedance spectroscopy (EIS) analyses were recorded at AC frequencies from 10 kHz to 0.1 Hz.

## 3. Results and Discussion

### 3.1. XRD Analysis

Figure 2 shows the XRD patterns of the Mn-doped  $\text{NiCo}_2\text{O}_4$  electrodes (a) without and (b) with ultrasonic-assisted samples at different molar ratios in the order of increasing Mn load (moving from samples A to F). Generally, standard  $\text{NiCo}_2\text{O}_4$  diffraction peaks (JCPDS No. 20-0781) could be observed for samples with and without ultrasonic assistance. A pure cubic  $\text{NiCo}_2\text{O}_4$  phase can be seen in Figure 2a, indicating that diffraction peaks of Mn alloys and other compounds were not in the samples. Two deviations from the XRD diffraction patterns were observed for those  $\text{NiCo}_2\text{O}_4$  samples doped with Mn, due to the different atomic radii of Ni (0.124 nm) and Mn (0.140 nm). The main diffraction

peak of the Mn-doped  $\text{NiCo}_2\text{O}_4$  electrode shifted significantly, and the crystallinities of the samples decreased as the manganese concentration in the reaction solution increased [17]. Sun et al. [30] reported that Mn atoms occupy Ni seats in  $\text{NiCo}_2\text{O}_4$  structures. According to the results of the XRD pattern, the major diffraction peaks of the  $\text{NiCo}_2\text{O}_4$  electrodes experienced a light shift with an increase in manganese concentration in the reaction solution, suggesting that the nickel sites were occupied by manganese atoms, with the  $\text{Mn}^{3+}$  ions preferring to replace the  $\text{Ni}^{3+}$  ions within  $\text{NiCo}_2\text{O}_4$ . This substitution improved the electronic structure and enhanced the ability for charge transfer, thereby improving the conductivity and efficiency of electron movement [28,31,32]. After doping with Mn, the ratio of Ni and Co atoms changed slightly, indicating that Mn atoms replaced the positions of Ni and Co. As Ni, Co, and Mn have different atomic radii (0.124, 0.167, and 0.140 nm, respectively), it is evident that Mn atoms replacing the positions of Ni and Co in a typical  $\text{NiCo}_2\text{O}_4$  electrode will result in slight deviations in the XRD diffraction of  $\text{NiCo}_2\text{O}_4$ . The structural representation of a typical  $\text{NiCo}_2\text{O}_4$  electrode demonstrates that Ni (or Mn) ions occupy octahedral sites, while Co ions occupy octahedral and tetragonal sites [17]. Interestingly, the electrical conductivity of electrodes can be improved to enhance electron transport, owing to the shift phenomenon of XRD, which can be attributed to the differences in the atomic radii of nickel and manganese.

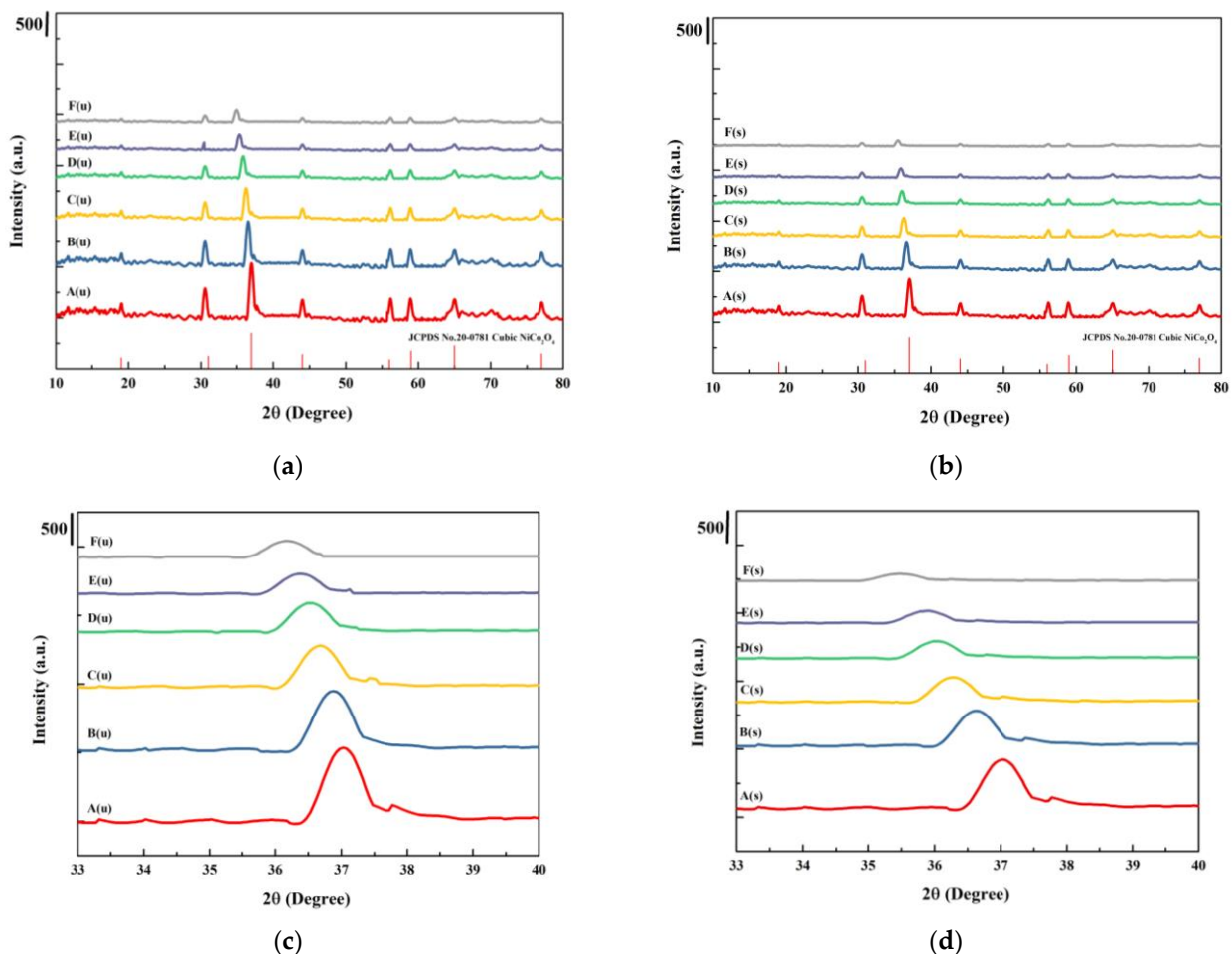


**Figure 2.** XRD patterns of Mn-doped  $\text{NiCo}_2\text{O}_4$  electrodes (a) without ultrasonic-assisted synthesis and (b) with ultrasonic-assisted synthesis. (c) Main peak without ultrasonic-assistance. (d) Main peak with ultrasonic-assistance.

A noticeable decrease in the crystallinities of the samples treated with ultrasound can be seen in Figure 2b. The intensity of the XRD diffraction patterns decreased due to the

smaller grain size in the ultrasonic-assisted samples [33]. The crystalline forms resulted in no changes in the samples. Based on the XRD results, the peak intensities of the samples that underwent ultrasonic-assisted synthesis were reduced by approximately 0.2 times compared to the original samples. Recently, numerous studies have reported that ultrasonic techniques can generate microturbulence, microjets, and shock waves and disrupt van der Waals forces, thereby enhancing the particle deagglomeration in solution systems and leading to more uniform particle size distribution. The grain size refinement of thin films can also be improved [34]. In addition, no impurities were found in the X-ray diffraction patterns. Based on the Scherrer formula, the crystallite sizes of  $\text{NiCo}_2\text{O}_4$  and Mn-doped  $\text{NiCo}_2\text{O}_4$  are listed in Table 2. The grain size of  $\text{NiCo}_2\text{O}_4$  was 16.92 nm for A(u) and 15.23 for A(s). The crystallite size of the Mn-doped  $\text{NiCo}_2\text{O}_4$  samples decreased as the concentration of the Mn doping increased with/without ultrasonic-assisted electrodeposition [35].

**Table 2.** Crystallite sizes of  $\text{NiCo}_2\text{O}_4$  and Mn-doped  $\text{NiCo}_2\text{O}_4$  samples.

Samples	Particle Size (nm)
A(u)	16.92
B(u)	16.11
C(u)	15.85
D(u)	15.21
E(u)	14.57
F(u)	14.13
A(s)	15.23
B(s)	14.50
C(s)	14.31
D(s)	13.62
E(s)	13.11
F(s)	12.75

(u) un-sonicated; (s) sonicated.

Figure 3 shows Raman spectra of the Mn-doped  $\text{NiCo}_2\text{O}_4$  electrodes. Raman peaks at 455, 505, and 648 align with the Raman peaks of  $\text{NiCo}_2\text{O}_4$ . No other phases or impurities were observed. Compared to Figure 3a,b, the peaks in Figure 3b had a negative shift, which means that the sample with ultrasonic-assisted synthesis had more oxygen vacancies [28]. The reduced Raman spectra intensities of the  $\text{NiCo}_2\text{O}_4$  phase were accompanied by an increased Mn concentration in the reaction.

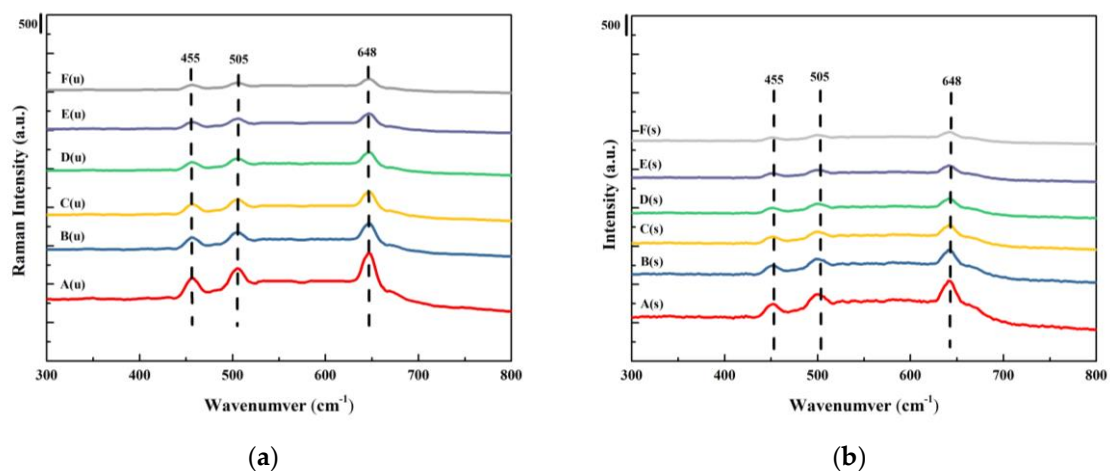


**Figure 3.** Raman spectra of Mn-doped  $\text{NiCo}_2\text{O}_4$  samples (a) without ultrasonic-assisted synthesis and (b) with ultrasound assisted-synthesis.

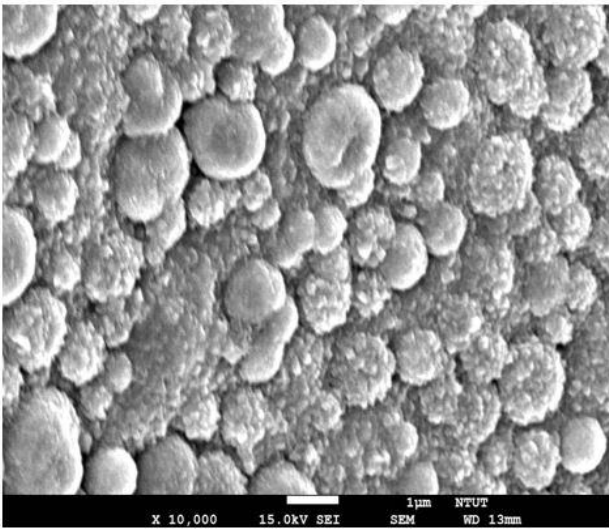
### 3.2. Morphology and XPS Analyses

Figure 4 shows the microstructure of the A(u) to F(s) samples at 10,000 $\times$  magnification. The microstructures of all of the samples changed from highly dense to porous due to various ultrasonic-assisted electrochemical deposition parameters in the electrodeposition reaction. The SEM results show that the morphology of the samples changed from a sphere to a tube to a sheet according to different Mn doping amounts. The ultrasound-treated sample showed smaller particles than the non-ultrasound-treated sample. The resulting morphologies are similar to those of Min et al. [36]. The microstructure could have become agglomerated and cracked as a result of an increased oxygen vacancy concentration in the samples [37]. Notably, the particle size was smaller than that of the samples without ultrasonic treatment, owing to the fact that aggregated cluster particles can be largely decreased by the ultrasonic conditions during electrodeposition [34]. The atomic ratios of the A(u) to F(s) samples are shown in Table 3. The atomic ratio values for Ni/Co/O/Mn were found to be 1.00:3.88/4.21:5.55/5.10:0/0.015. While the atomic ratios of Mn increased in the samples, the ratios of Co/Ni increased gradually. Additionally, all of the samples were prepared under oxygen-poor conditions with an increased concentration of Mn in the electrodeposition reaction, meaning that the oxygen vacancy defects were caused by doping of the Mn element [36]. Replacement of the Ni element by Mn caused oxygen vacancy defects, indicated in the EDS results by the ratio of Mn increasing while the ratio of O decreased. To provide evidence of oxygen deficiency, XPS analysis was conducted. Figure 5 shows the XPS spectra of F(u) and F(s) obtained with and without ultrasonic-assisted electrodeposition to confirm oxygen deficiencies and the replacement of Ni by Mn. An increase in the peak area for O 1s (531.63 eV) was observed for F(s), indicating that the ultrasonic-assisted synthesis successfully introduced abundant oxygen vacancies [38]. Figure 6 shows the XPS spectra of A(u) and F(u), both before and after Mn doping for Mn 2p, Co 2p, Ni 2p, and O 1s. When Mn was doped, the XPS strength of Co and Ni in F(s) significantly decreased due to the decrease in their content. On the contrary, the XPS strength of O 1s increased due to the rise in oxygen vacancies present in F(s). These findings are consistent with the trends observed in the XRD analysis [38].

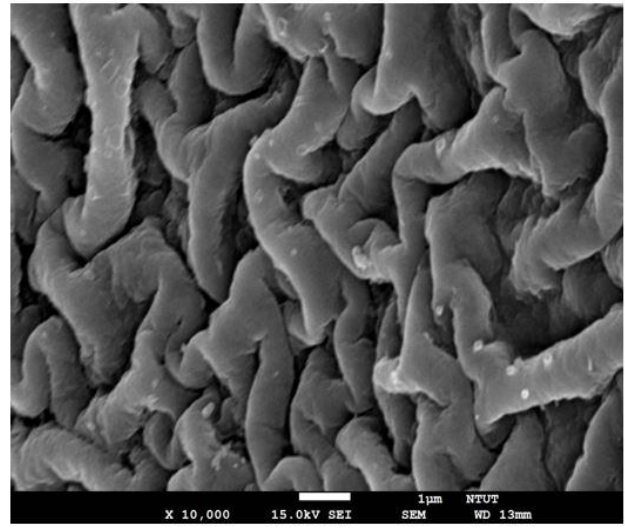
**Table 3.** Atomic ratios of Ni:Co:O:Mn from sample A(u) to sample F(s).

Sample	Mole Ratios of Ni:Co:Mn	Atomic Ratios of Ni:Co:O:Mn
A(u)	1:1:0.0	1:3.88:5.55:0.000
B(u)	1:1:0.2	1:3.91:5.45:0.005
C(u)	1:1:0.4	1:3.96:5.31:0.007
D(u)	1:1:0.6	1:4.05:5.21:0.009
E(u)	1:1:0.8	1:4.11:5.12:0.012
F(u)	1:1:1.0	1:4.21:5.10:0.015
A(s)	1:1:0.0	1:3.90:5.53:0.000
B(s)	1:1:0.2	1:3.93:5.49:0.005
C(s)	1:1:0.4	1:4.01:5.35:0.008
D(s)	1:1:0.6	1:4.07:5.21:0.010
E(s)	1:1:0.8	1:4.13:5.15:0.013
F(s)	1:1:1.0	1:4.19:5.09:0.015

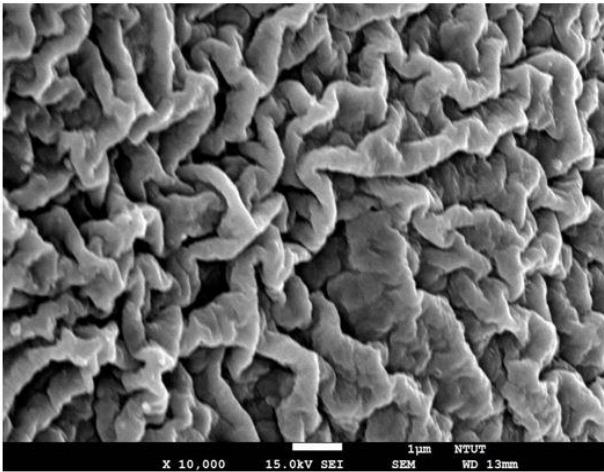
(u) un-sonicated; (s) sonicated.



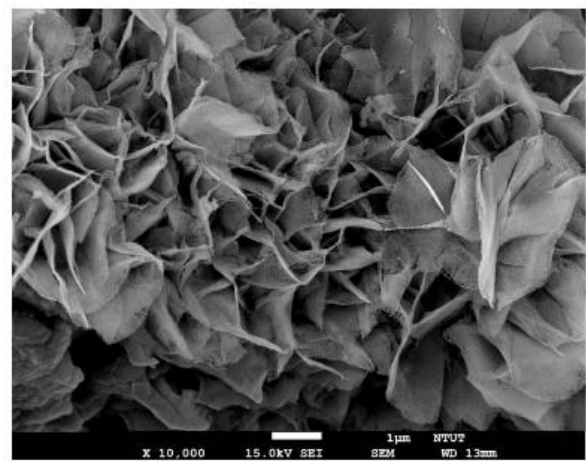
A(u)



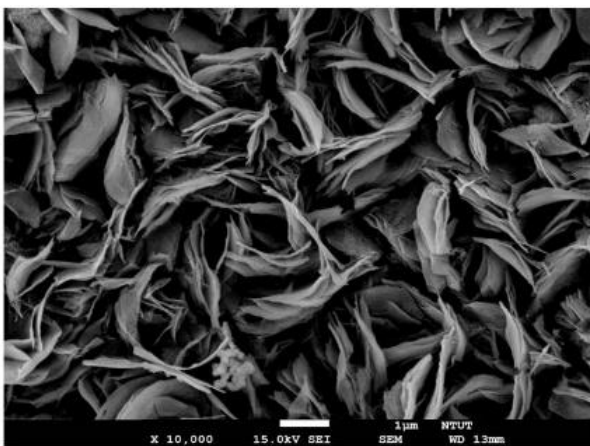
B(u)



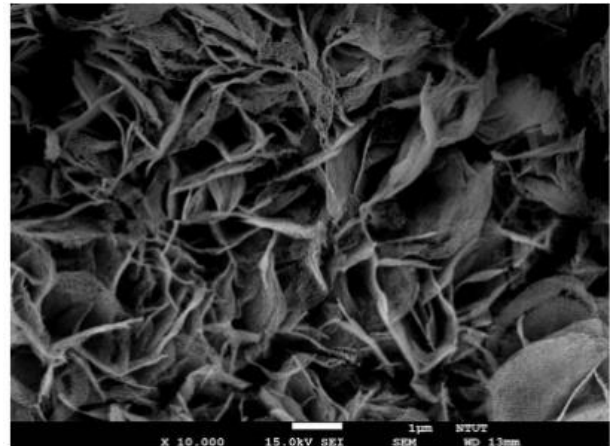
C(u)



D(u)

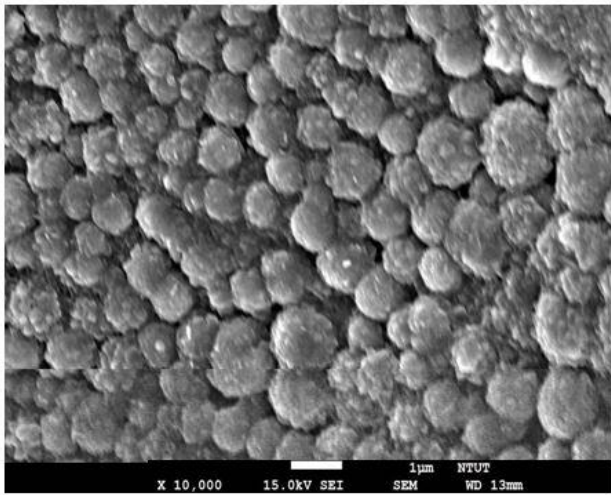


E(u)

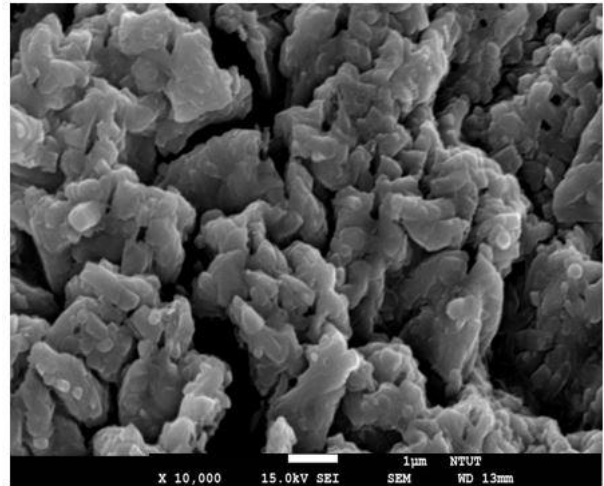


F(u)

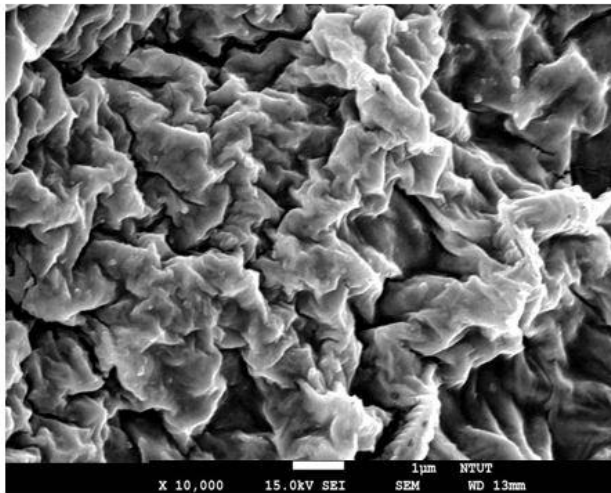
Figure 4. Cont.



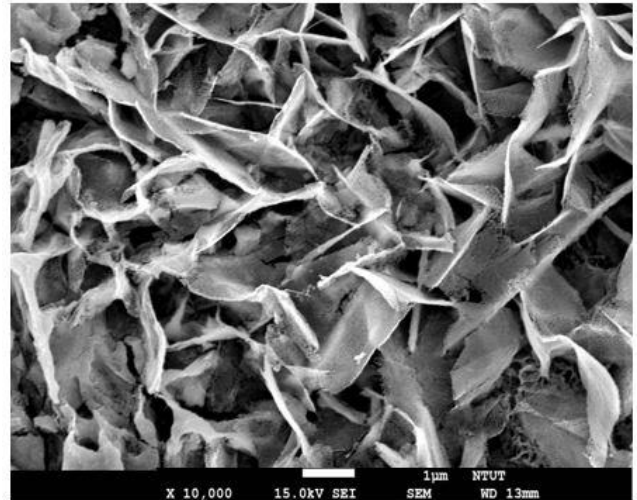
A(s)



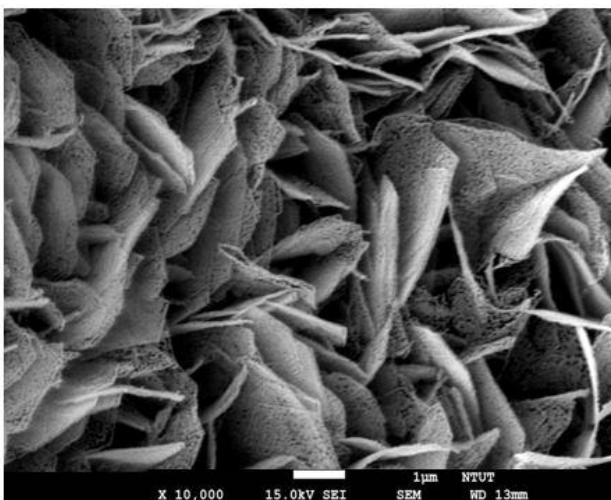
B(s)



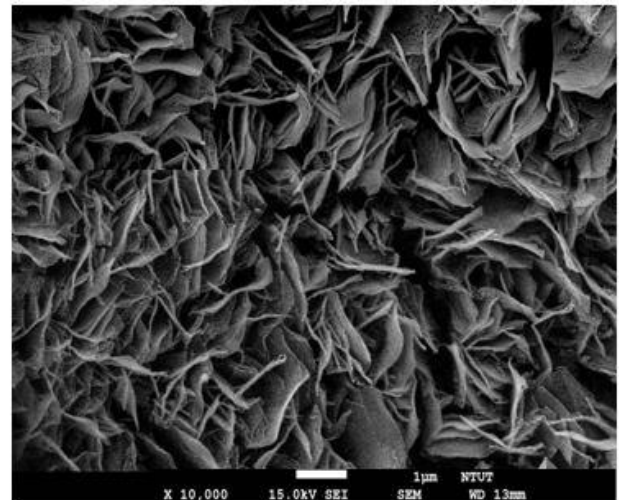
C(s)



D(s)



E(s)



F(s)

**Figure 4.** SEM images of samples A(u)–F(u) and for A(s)–F(s). at a magnification of 10,000 $\times$ .

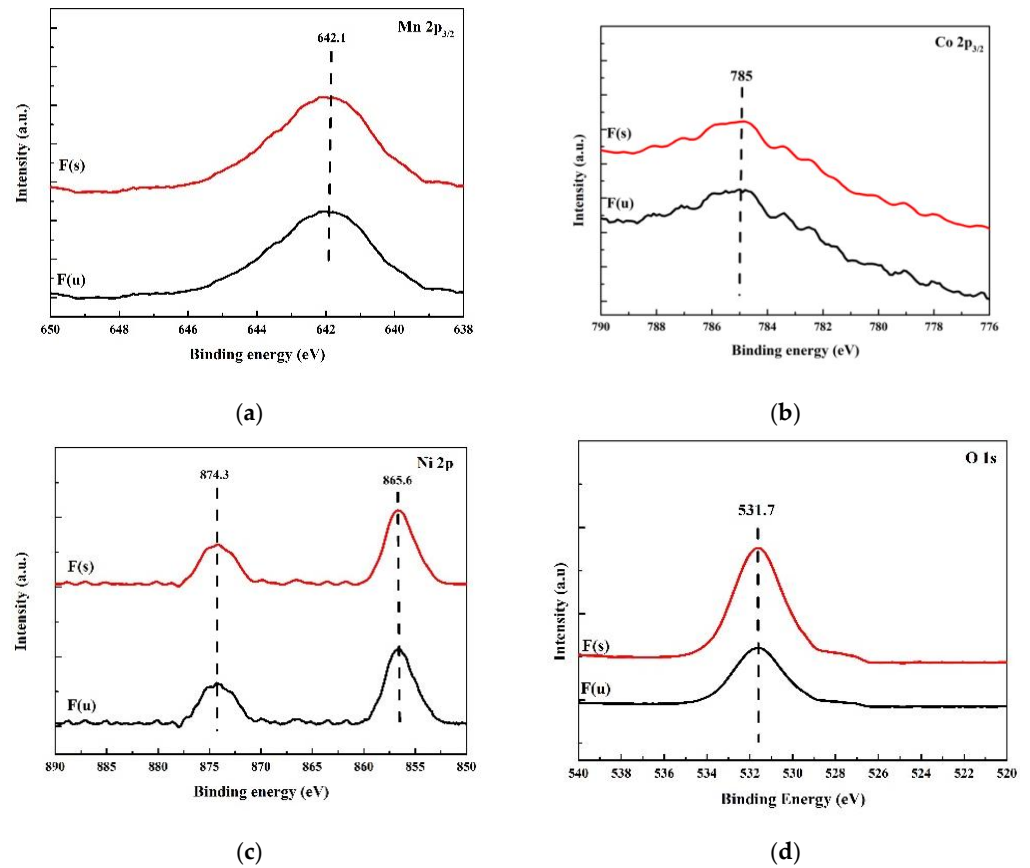


Figure 5. XPS survey patterns of F(u) and F(s): (a) Mn 2p, (b) Co 2p, (c) Ni 2p, (d) O 1s.

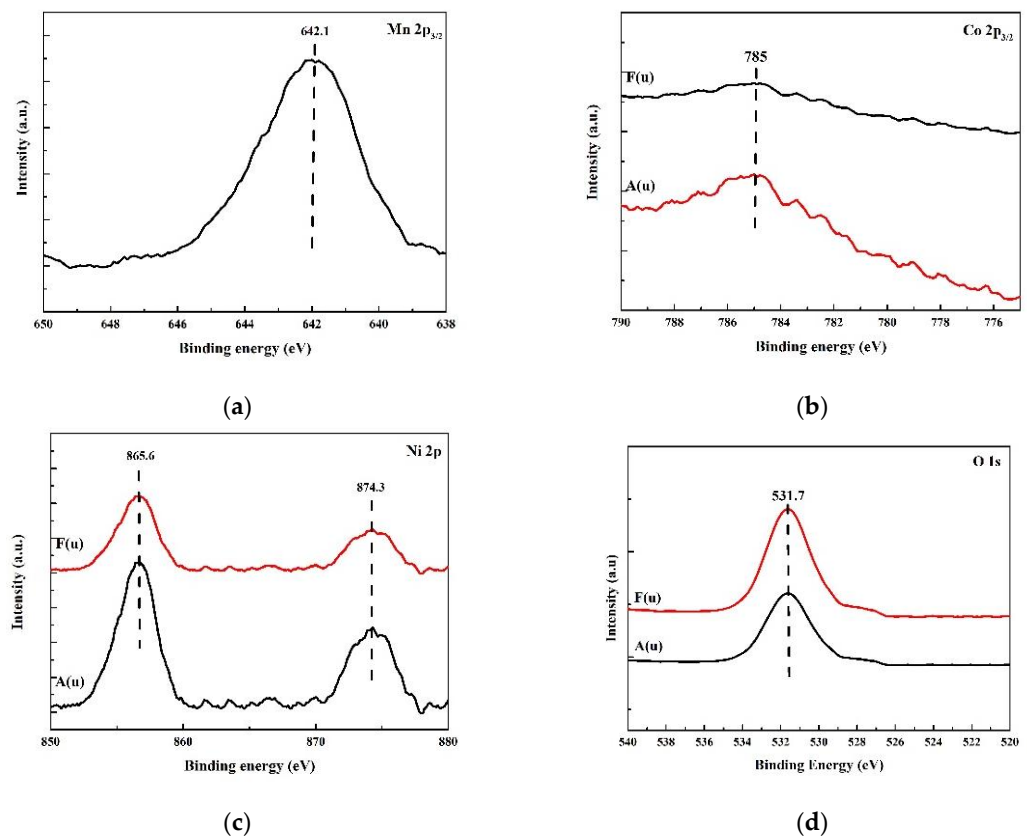
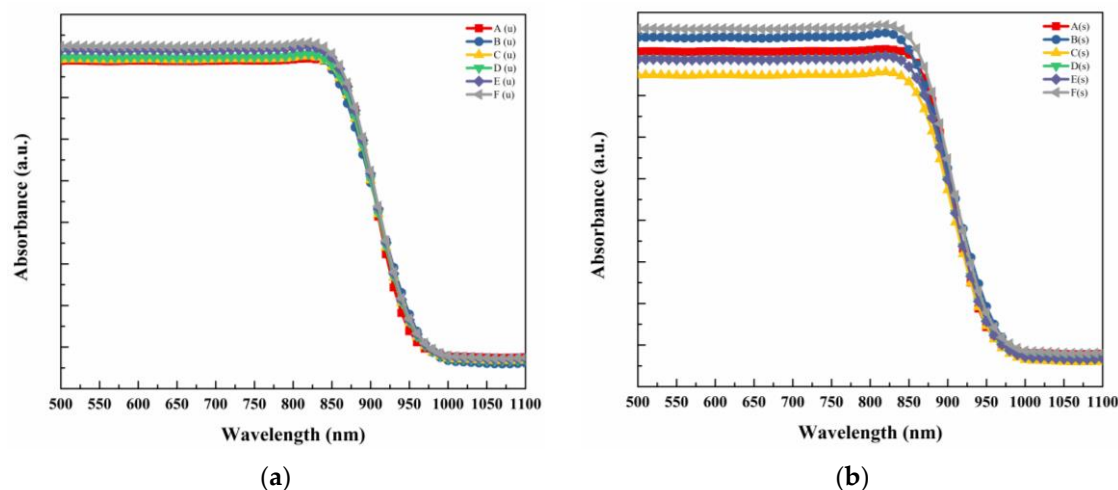


Figure 6. Mn 2p, Co 2p, Ni 2p, and O 1s XPS spectra of A(u) and F(u): (a) Mn 2p, (b) Co 2p, (c) Ni 2p, (d) O 1s.

### 3.3. UV–Vis Diffuse Reflectance Spectroscopy Analysis

Figure 7a,b show the UV diffuse reflectance spectroscopy of the A(u) to F(s) samples. All of the samples demonstrated absorption of the visible light range. The value of the absorption edges of the samples was around 920 nm (1.35 eV). The Mn-doped  $\text{NiCo}_2\text{O}_4$  samples that underwent ultrasonic-assisted treatment had the same band gap, corroborating the value of 1.35 V found by Wan et al. [13].



**Figure 7.** UV diffuse reflectance spectroscopy of Mn-doped  $\text{NiCo}_2\text{O}_4$  electrodes: (a) samples without ultrasonic-assisted synthesis; (b) samples with ultrasonic-assisted synthesis.

### 3.4. Porosity and Surface Area Characterization

The nitrogen adsorption and desorption isotherms of the A(u) to F(s) samples are shown in Figure 8a,b. The hysteresis loop curves of all of the samples were IV isotherms, indicating that the Mn-doped  $\text{NiCo}_2\text{O}_4$  electrodes were a classic mesoporous type. The relative pressure at 0.9 among all of the samples experienced sharp growth, showing an increase in the adsorbed volume and capillary condensation, which was carried out in the nitrogen adsorption isotherm system. Xing et al. [39] reported that the  $\text{H}_2$ -type hysteresis loop of a steep triangular desorption branch can provide highly interconnected ink-bottle-like pores. Table 4 shows the textural properties of the Mn-doped  $\text{NiCo}_2\text{O}_4$ . The increased surface area was due to the microstructure transfer from a highly dense structure to a porous structure with gradually increased doping of manganese elements in the electrodeposition reaction. As shown in Table 4, it can be concluded that the order of the specific surface area is  $F(u) > E(u) > D(u) > C(u) > B(u) > A(u)$ . These results indicate that the surface area of those samples without ultrasonic assistance could be improved through doping with manganese. Additionally, the surface area of those samples with ultrasonic-assisted synthesis in the electrodeposition reaction was higher than those samples without ultrasonic-assisted synthesis, owing to the mass transfer at the particle surface, which can be improved during the mixing of pre-cursors for electrodeposition reaction systems [40]. The textural properties of the Mn-doped  $\text{NiCo}_2\text{O}_4$  were determined using the BET equation and the Barrett–Joyner–Halenda (BJH) model, based on the nitrogen adsorption and desorption isotherms among all of the samples. The pore volume, pore size, and surface area of the Mn-doped  $\text{NiCo}_2\text{O}_4$  samples without ultrasonic-assisted treatment were 0.49–0.82  $\text{cm}^3/\text{g}$ , 120–170 Å, and 65.11–126.54  $\text{m}^2/\text{g}$ , respectively, indicating that the textural properties belong to hierarchical porous structures. Figure 9 shows the pore size distributions of all of the samples obtained via calculation using the BJH approach. Interestingly, the mesoporous structure of narrower pores (3 to 100 nm) could be detected among those electrodes with ultrasonic-assisted preparation. In contrast, the central pore size distribution of those electrodes without ultrasonic-assisted preparation was around 48 nm, which increased to the macropore range. Hao et al. [26] reported ideal materials

that have hierarchical macroporous structures to transport electrons and ions efficiently for excellent photoactivity. The textural properties of the samples agreed with the morphology results. The surface area of the Mn-doped NiCo<sub>2</sub>O<sub>4</sub> samples with ultrasonic-assisted treatment was higher than that of the A(u) to F(u) samples, largely because ultrasonic treatment provided an effective method to improve ion deposition compatibility through the leveling effect [22]. Costa et al. [28] reported that the particle deagglomeration in the electrodeposition process combined with the ultrasound technique could be promoted due to microturbulence, microjets, shock waves, and van der Waals forces causing physical and chemical property changes. However, large aggregates of particles in the electrodes in the plating solution could be observed and incorporated inside the thin films [37].

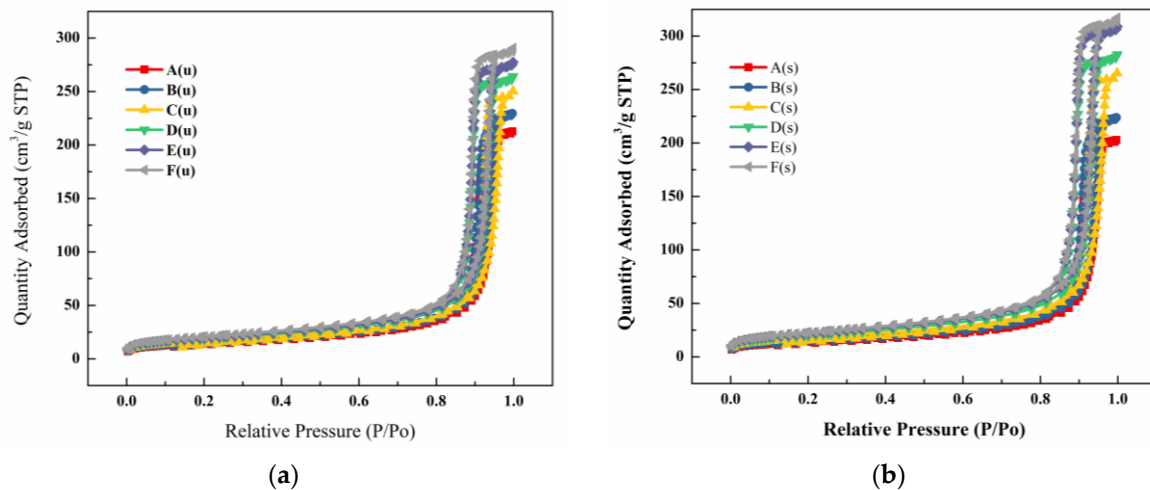


**Figure 8.** The hysteresis loop for electrodes between nitrogen adsorption and desorption isotherms: (a) samples without ultrasonic-assisted synthesis; (b) samples with ultrasonic-assisted synthesis.

**Table 4.** Textural properties of Mn-doped NiCo<sub>2</sub>O<sub>4</sub> electrodes.

Samples	Surface Area (m <sup>2</sup> /g)	Pore Volume (cm <sup>3</sup> /g)	Pore Size (Å)
A(u)	65.11	0.49	120
B(u)	70.32	0.51	135
C(u)	80.56	0.62	146
D(u)	95.35	0.69	150
E(u)	102.36	0.75	155
F(u)	112.45	0.82	157
A(s)	84.12	0.56	145
B(s)	90.23	0.62	153
C(s)	98.54	0.73	162
D(s)	112.35	0.78	166
E(s)	126.54	0.82	170
F(s)	130.21	0.91	173

(u) un-sonicated; (s) sonicated.

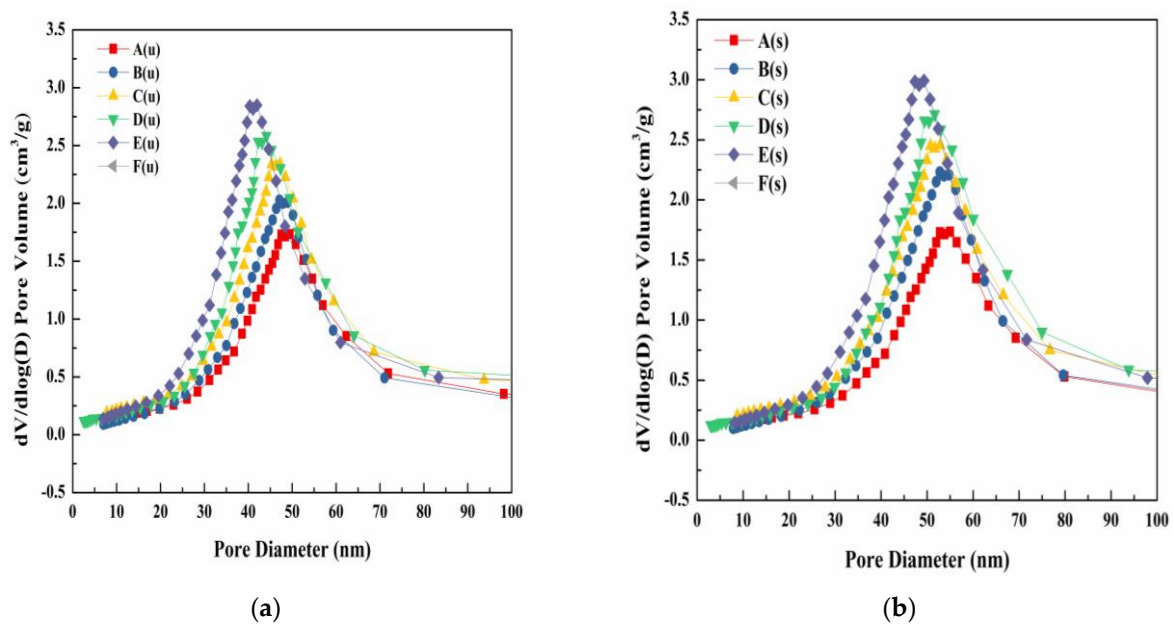


**Figure 9.** Pore size distribution for (a) samples without ultrasonic—assisted synthesis and (b) samples with ultrasonic—assisted synthesis.

### 3.5. Photocatalytic Activity Evaluation

Figure 10 shows the photodegradation of the methyl red solution of all of the samples with a 1.35 eV band gap. As seen in Figure 10, the F(s) sample showed the highest photocatalytic degradation, amounting to approximately 90% of methyl red degradation among all of the samples. Table 4 shows the first-order rate constant of all of the samples using the Langmuir–Hinshelwood kinetic model. The value of the first-order rate constant for those samples without ultrasonic-assisted synthesis increased in the order  $F(u) > E(u) > D(u) > C(u) > B(u) > A(u)$  when comparing the value of the first-order rate constant for those samples without ultrasonic-assisted synthesis, which is in agreement with the order of the textural property results. The first-order rate constant was improved from 0.0055 to  $0.0063 \text{ min}^{-1}$  when the preparation of the electrode was accompanied by ultrasound. As seen in Table 5, it is noteworthy that the first-order rate constant, with an increase in the oxygen vacancy concentration and a high surface area, was in the order of  $F(s) > E(s) > D(s) > C(s) > B(s) > A(s)$ , owing to the large surface area and nano-size particles of the thin films. This situation may be attributed to the dispersion of the metal catalyst upon ultrasonic treatment, improving the overall surface area and hence improving photocatalytic performance, including the crystalline structures, microstructures, and defect levels in the nanomaterials, which can be controlled by means of ultrasonic assistance in the electrodeposition reaction. Additionally, the F(s) sample exhibited the best photocatalytic performance in degrading methyl red among all of the samples, indicating that a special mesoporous structure and high surface area improve the abilities of light harvesting and methyl red adsorption. The enhancement in the photodegradation performance of the Mn-doped  $\text{NiCo}_2\text{O}_4$  samples prepared via ultrasonic-assisted electrodeposition [39] might be due to their high surface area and defect properties.

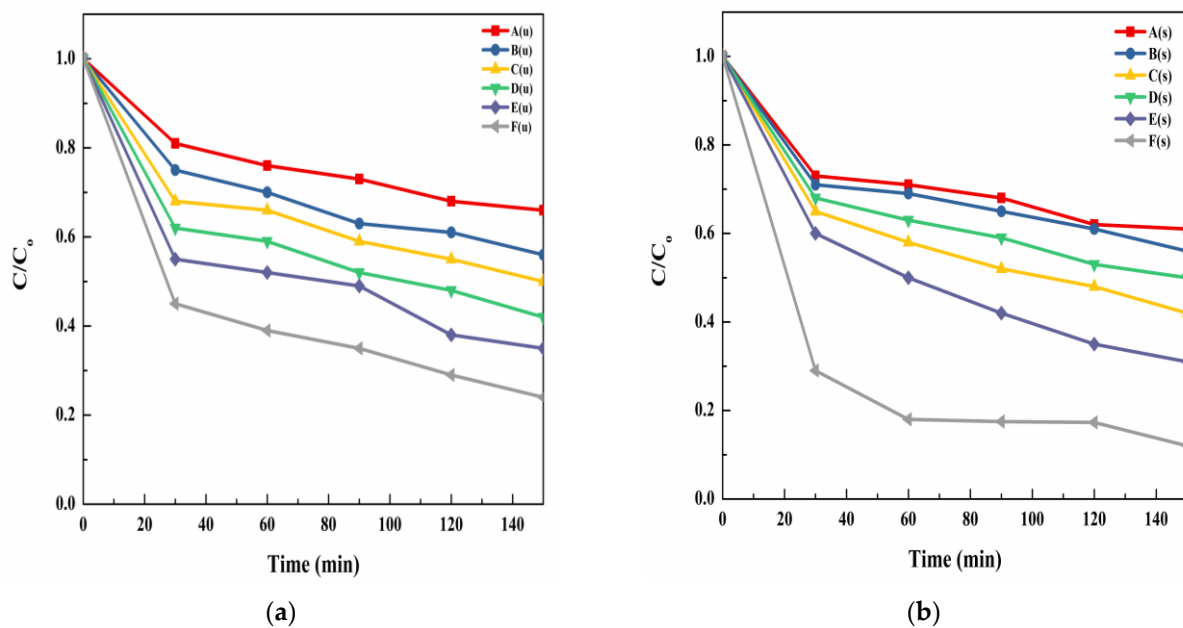


**Figure 10.** Photodegradation of methyl red solution by Mn-doped NiCo<sub>2</sub>O<sub>4</sub> samples (a) without ultrasonic-assisted synthesis and (b) with ultrasound assisted-synthesis.

**Table 5.** The first-order rate constant of all samples as measured by the Langmuir–Hinshelwood kinetic model.

Samples	First-Order Rate Constant (min <sup>-1</sup> )
A(u)	0.0016
B(u)	0.0023
C(u)	0.0030
D(u)	0.0037
E(u)	0.0048
F(u)	0.0055
A(s)	0.0018
B(s)	0.0025
C(s)	0.0035
D(s)	0.0041
E(s)	0.0054
F(s)	0.0063

(u) un-sonicated; (s) sonicated.

The hydroxyl groups of the Mn-doped NiCo<sub>2</sub>O<sub>4</sub> samples played a significant role in the photodegradation of the methyl red solution. To further explain the hydroxyl groups in the photocatalysts, the photocatalysts were put in the DRIFT and heated from room temperature to 250 °C to remove the adsorbed water from the photocatalyst’s surface. A broad and strong band from 3000 to 3700 cm<sup>-1</sup> among the samples can be observed in Figure 11. The F(s) sample had the strongest hydroxyl group band among all of the samples, meaning that the Brønsted acidity properties and chemical adsorption on the photocatalytic surface can be improved by employing ultrasonic-assisted synthesis. Salam [41] reported that a tunable pore architecture with richer OH groups can be obtained via ultrasound to enhance the interaction capacity of the atoms, ions, and molecules in photocatalysts. The F(s) sample had the highest photocatalytic performance among all of the samples, with an excellent crystalline and microporous structure, the highest surface area, and the strongest hydroxyl groups band. The hydrogen evolution of all of the samples is shown in Figure 12. During the hydrogen evolution, the F(s) sample had the maximum value (38 μmol/cm<sup>2</sup>) among all of the samples based on 300 W Xe lamp irradiation. It was around 1.9 times higher than that of the F(u) sample. The highest hydrogen production efficiency

was mainly attributed to the improved electrical conductance, meaning that the Ni atoms were substituted with Mn atoms to form donor-type defects. The number of Mn sites in the crystal lattice under ultrasonic-assisted synthesis was higher than that in the sample without ultrasonic-assisted synthesis.

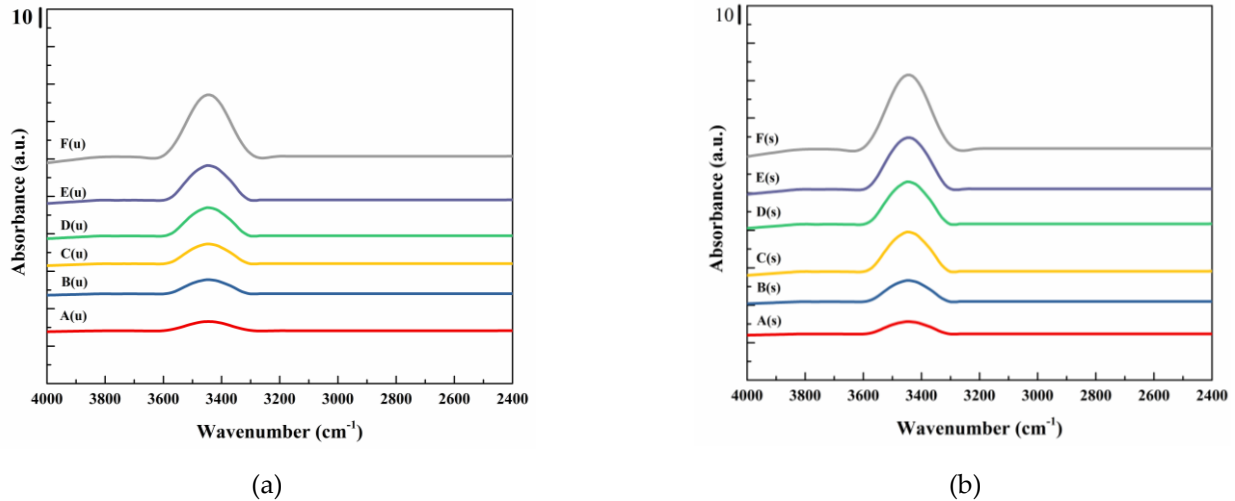


**Figure 11.** FTIR spectra of Mn-doped NiCo<sub>2</sub>O<sub>4</sub> samples (a) without ultrasonic-assisted synthesis and (b) with ultrasound assisted-synthesis.

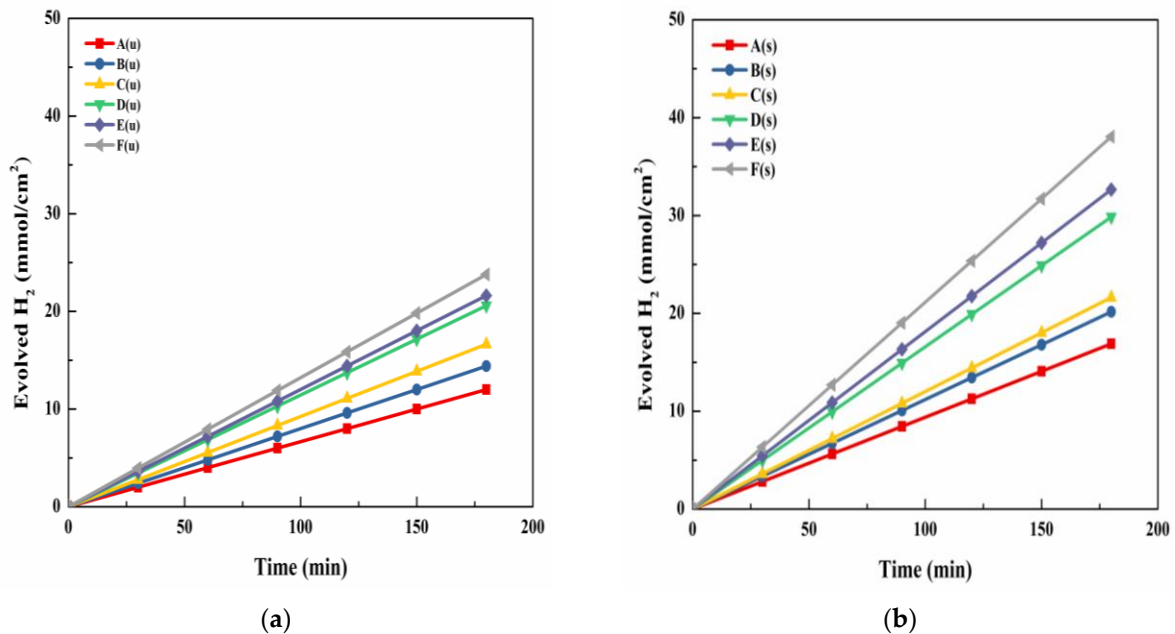


**Figure 12.** The hydrogen evolution performance of Mn-doped NiCo<sub>2</sub>O<sub>4</sub> samples (a) without ultrasonic-assisted synthesis and (b) with ultrasonic-assisted synthesis.

### 3.6. Electrochemical Performance of the Mn-Doped NiCo<sub>2</sub>O<sub>4</sub> Electrodes

A three-electrode setup was used to analyze the electrochemical behavior of the synthesized Mn-doped NiCo<sub>2</sub>O<sub>4</sub> electrodes. The results of the galvanostatic charge and discharge (GCD), cyclic voltammetry (CV), and electrochemical impedance spectroscopy (EIS) analyses are shown in Figure 13. The average specific capacitance of the samples can be calculated from the CV curves by integrating the area under the current–potential curve:

$$C = \frac{1}{mv(V_c - V_a)} \int_{V_a}^{V_c} I(V)dV$$

where  $C$  is the specific capacitance ( $F g^{-1}$ ),  $m$  is the mass of the active material in the electrode,  $n$  is the potential scan rate ( $mVs^{-1}$ ),  $V_c - V_a$  is the potential window, and  $I(V)$  is the response current (mA) [42].

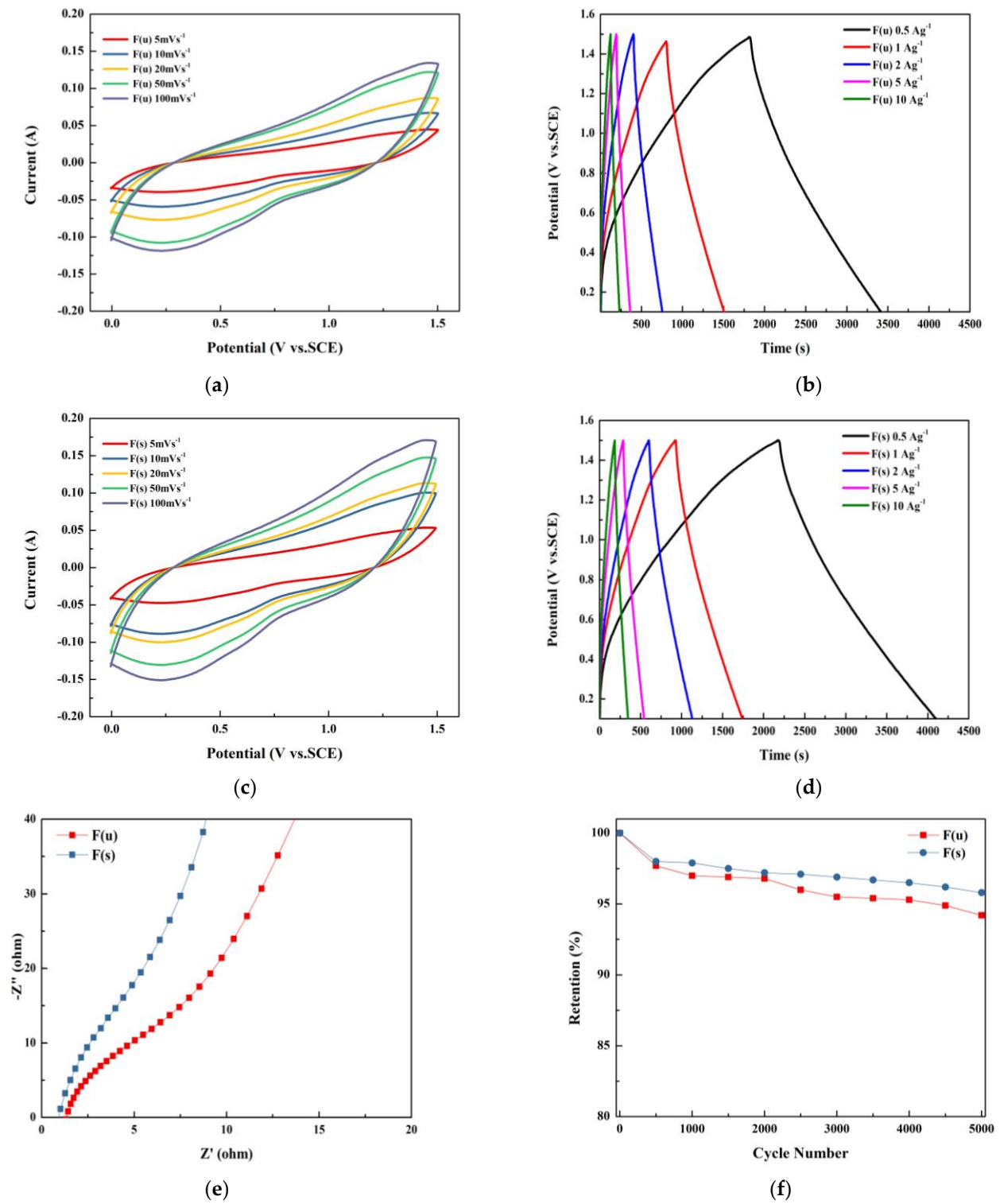
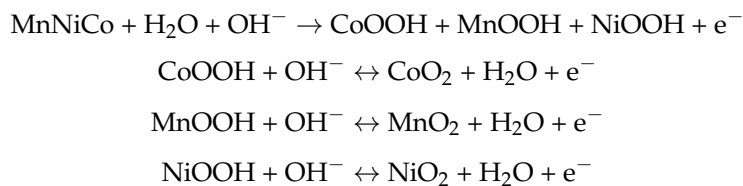


**Figure 13.** Electrochemical properties of Mn-doped  $NiCo_2O_4$  electrodes: (a) CV curves of sample F(u); (b) GCD of sample F(u); (c) CV curves of sample F(s); (d) GCD of sample F(s); (e) EIS values of F(s) and F(u); (f) capacity retention rate of sample F(s) and F(u).

The mechanism of redox conversions at Mn-doped NiCo<sub>2</sub>O<sub>4</sub> electrodes in KOH electrolyte could be represented as follows:



The potentials of all these redox reactions are very close, so all the redox peaks merge into one. Therefore, only one peak can be observed in the CV curve. The redox peaks are mainly attributed to redox reactions associated with N-O/N-O-OH (where N stands for Co, Ni, or Mn). Samples synthesized with ultrasound assistance showed stronger redox reactions than those without. The excellent performance of the ultrasonic-assisted synthesized sample is mainly attributed to its higher specific surface area, which reduces its intrinsic resistance and thus leads to better electrochemical performance [43,44].

Table 6 presents the specific capacitance values and intrinsic resistance values for electrodes from the F(u) (192 F g<sup>-1</sup>, 1.3 Ω) and F(s) (260 F g<sup>-1</sup>, 0.8 Ω) samples; the ultrasonic-assisted synthesis results showed superior capacitance and lower impedance. In Figure 13f, capacitance retention was tested under a current of 1 Ag<sup>-1</sup> for 5000 cycles; the retention of the F(u) and F(s) samples was 94% and 96%, respectively, showing good asymmetric supercapacitor electrode potential.

**Table 6.** Specific capacitance values of Mn-doped NiCo<sub>2</sub>O<sub>4</sub> electrodes obtained from cyclic voltammetry study and the intrinsic resistance of electrodes (Rs) from electrochemical impedance spectra.

Samples	Scan Rate (V/s)	Capacity (F/g)	Intrinsic Resistance of Electrode (Ω)	Retention Rate after 5000 Cycles Test
F(u)	0.05	192	1.3	94%
F(s)	0.05	260	0.8	96%

(u) un-sonicated; (s) sonicated.

#### 4. Conclusions

This study demonstrated the hydrogen evolution, photodegradation, and supercapacitor electrochemical properties of Mn-doped NiCo<sub>2</sub>O<sub>4</sub> electrodes prepared via ultrasonic-assisted electrodeposition. This study has two distinctive features: (1) it introduced a rapid and efficient method for modifying/introducing oxygen vacancies in electrodes, and (2) it encompassed a comprehensive set of characterizations for hydrogen evolution, photodegradation, and supercapacitor performance. The preparation parameters were varied to achieve different degrees of oxygen vacancies, and comparisons were made with and without the use of ultrasound assistance. Increasing oxygen vacancies altered the microstructure of the electrodes, forming layered 3D flower-like porous nanoplates and enhancing the specific surface area and carrier density. Applying ultrasonic-assisted technology resulted in the lowest AC resistance and highest charge transfer efficiency. Consequently, the Mn-doped NiCo<sub>2</sub>O<sub>4</sub> electrodes with the richest oxygen vacancies prepared by means of ultrasonic-assisted electrodeposition exhibited the highest hydrogen evolution, photodegradation efficiency, and electrochemical performance.

**Author Contributions:** K.-C.L.: methodology, writing—original draft. T.J.T.: conceptualization. G.-T.P.: validation, formal analysis. T.C.-K.Y.: conceptualization. K.U.: data curation. Z.-L.T.: data curation, Resources. A.N.N.: validation. C.-M.H.: writing—review and editing. All authors have read and agreed to the published version of the manuscript.

**Funding:** This work was financially supported by the National Science and Technology Council (NSTC) of Taiwan under project NSTC 112-2637-E-168-007. The authors gratefully acknowledge the

use of code XRD005100 and use of the machine equipment belonging to the Core Facility Center of National Cheng Kung University.

**Data Availability Statement:** Data are contained within the article.

**Conflicts of Interest:** We certify that the submission is original work and is not under review at any other publication. Hence, we declare no conflict of interest.

## References

1. El Sharkawy, H.M.; Shawky, A.M.; Elshypany, R.; Selim, H. Efficient photocatalytic degradation of organic pollutants over TiO<sub>2</sub> nanoparticles modified with nitrogen and MoS<sub>2</sub> under visible light irradiation. *Sci. Rep.* **2023**, *13*, 8845. [[CrossRef](#)]
2. Kale, G.; Arbuj, S.; Chothe, U.; Khore, S.; Nikam, L.; Kale, B. Highly Crystalline Ordered Cu-doped TiO<sub>2</sub> Nanostructure by Paper Templated Method: Hydrogen Production and Dye Degradation under Natural Sunlight. *J. Compos. Sci.* **2020**, *4*, 48. [[CrossRef](#)]
3. Pan, X.; Yang, M.-Q.; Fu, X.; Zhang, N.; Xu, Y.-J. Defective TiO<sub>2</sub> with oxygen vacancies: Synthesis, properties and photocatalytic applications. *Nanoscale* **2013**, *5*, 3601–3614. [[CrossRef](#)]
4. Bi, X.; Du, G.; Kalam, A.; Sun, D.; Yu, Y.; Su, Q.; Xu, B.; Al-Sehemi, A.G. Tuning oxygen vacancy content in TiO<sub>2</sub> nanoparticles to enhance the photocatalytic performance. *Chem. Eng. Sci.* **2021**, *234*, 116440. [[CrossRef](#)]
5. Dubey, R.S.; Jadkar, S.R.; Bhorde, A.B. Synthesis and characterization of various doped TiO<sub>2</sub> nanocrystals for dye-sensitized solar cells. *ACS Omega* **2021**, *6*, 3470–3482. [[CrossRef](#)]
6. Basavarajappa, P.S.; Patil, S.B.; Ganganagappa, N.; Reddy, K.R.; Raghu, A.V.; Reddy, C.V. Recent progress in metal-doped TiO<sub>2</sub>, non-metal doped/codoped TiO<sub>2</sub> and TiO<sub>2</sub> nanostructured hybrids for enhanced photocatalysis. *Int. J. Hydrog. Energy* **2020**, *45*, 7764–7778. [[CrossRef](#)]
7. Erusappan, E.; Pan, G.-T.; Chung, H.-Y.; Chong, S.; Thiripuranthagan, S.; Yang, T.C.-K.; Huang, C.-M. Hierarchical nickel–cobalt oxide and glucose-based carbon electrodes for asymmetric supercapacitor with high energy density. *J. Taiwan Inst. Chem. Eng.* **2020**, *112*, 330–336. [[CrossRef](#)]
8. Herrmann, J.-M.; Tahiri, H.; Ait-Ichou, Y.; Lassaletta, G.; Gonzalez-Elipe, A.; Fernandez, A. Characterization and photocatalytic activity in aqueous medium of TiO<sub>2</sub> and Ag-TiO<sub>2</sub> coatings on quartz. *Appl. Catal. B Environ.* **1997**, *13*, 219–228. [[CrossRef](#)]
9. Moon, J.; Takagi, H.; Fujishiro, Y.; Awano, M. Preparation and characterization of the Sb-doped TiO<sub>2</sub> photocatalysts. *J. Mater. Sci.* **2001**, *36*, 949–955. [[CrossRef](#)]
10. Anpo, M.; Takeuchi, M. The design and development of highly reactive titanium oxide photocatalysts operating under visible light irradiation. *J. Catal.* **2003**, *216*, 505–516. [[CrossRef](#)]
11. Umebayashi, T.; Yamaki, T.; Yamamoto, S.; Miyashita, A.; Tanaka, S.; Sumita, T.; Asai, K. Sulfur-doping of rutile-titanium dioxide by ion implantation: Photocurrent spectroscopy and first-principles band calculation studies. *J. Appl. Phys.* **2003**, *93*, 5156–5160. [[CrossRef](#)]
12. Cui, B.; Lin, H.; Liu, Y.Z.; Li, J.B.; Sun, P.; Zhao, X.C.; Liu, C.J. Photophysical and photocatalytic properties of core-ring structured NiCo<sub>2</sub>O<sub>4</sub> nanoplatelets. *J. Phys. Chem. C* **2009**, *113*, 14083–14087. [[CrossRef](#)]
13. Wan, Y.; Chen, J.; Zhan, J.; Ma, Y. Facile synthesis of mesoporous NiCo<sub>2</sub>O<sub>4</sub> fibers with enhanced photocatalytic performance for the degradation of methyl red under visible light irradiation. *J. Environ. Chem. Eng.* **2018**, *6*, 6079–6087. [[CrossRef](#)]
14. Gaim, Y.T.; Yimanuh, S.M.; Kidanu, Z.G. Enhanced photocatalytic degradation of amoxicillin with MN-doped Cu<sub>2</sub>O under sunlight irradiation. *J. Compos. Sci.* **2022**, *6*, 317. [[CrossRef](#)]
15. Omarova, A.Z.; Ayazbaev, T.; Yesdauletova, Z.S.; Aldabergen, S.A.; Kozlovskiy, A.L.; Moldabayeva, G.Z. Evaluation of the Applicability of Modifying CdSe Thin Films by the Addition of Cobalt and Nickel to Enhance the Efficiency of Photocatalytic Decomposition of Organic Dyes. *J. Compos. Sci.* **2023**, *7*, 460. [[CrossRef](#)]
16. Han, X.; Song, L.; Ding, J.; Hu, L.; Xu, C.; Wang, Y. Design and preparation of Cu-doped NiCo<sub>2</sub>O<sub>4</sub> nanosheets with intrinsic porosities for symmetric supercapacitors. *Mater. Lett.* **2020**, *278*, 128400. [[CrossRef](#)]
17. Van Nguyen, T.; Van Thuy, V.; Thao, V.D.; Hatsukano, M.; Higashimine, K.; Maenosono, S.; Chun, S.E.; Thu, T.V. Facile synthesis of Mn-doped NiCo<sub>2</sub>O<sub>4</sub> nanoparticles with enhanced electrochemical performance for a battery-type supercapacitor electrode. *Dalton Trans.* **2020**, *49*, 6718–6729. [[CrossRef](#)]
18. Pradeepa, S.; Rajkumar, P.; Diwakar, K.; Sutharthani, K.; Subadevi, R.; Sivakumar, M. A Facile One-Pot Hydrothermal Synthesis of Zn, Mn Co-Doped NiCo<sub>2</sub>O<sub>4</sub> as an Efficient Electrode for Supercapacitor Applications. *Chem. Sel.* **2021**, *6*, 6851–6862. [[CrossRef](#)]
19. Liang, Z.; Tu, H.; Kong, Z.; Yao, X.; Xu, D.; Liu, S.; Shao, Y.; Wu, Y.; Hao, X. Urchin like inverse spinel manganese doped NiCo<sub>2</sub>O<sub>4</sub> microspheres as high performances anode for lithium-ion batteries. *J. Colloid Interface Sci.* **2022**, *616*, 509–519. [[CrossRef](#)]
20. Hong, Z.-Y.; Chen, L.-C.; Li, Y.-C.M.; Hsu, H.-L.; Huang, C.-M. Response Surface Methodology Optimization in High-Performance Solid-State Supercapattery Cells Using NiCo<sub>2</sub>S<sub>4</sub>–Graphene Hybrids. *Molecules* **2022**, *27*, 6867. [[CrossRef](#)]
21. Hsieh, M.-C.; Chen, B.-H.; Hong, Z.-Y.; Liu, J.-K.; Huang, P.-C.; Huang, C.-M. Fabrication of 5 V High-Performance Solid-State Asymmetric Supercapacitor Device Based on MnO<sub>2</sub>/Graphene/Ni Electrodes. *Catalysts* **2022**, *12*, 572. [[CrossRef](#)]
22. Ismail, M.M.; Hong, Z.-Y.; Arivanandhan, M.; Yang, T.C.-K.; Pan, G.-T.; Huang, C.-M. In Situ binder-free and hydrothermal growth of nanostructured NiCo<sub>2</sub>S<sub>4</sub>/Ni electrodes for solid-state hybrid supercapacitors. *Energies* **2021**, *14*, 7114. [[CrossRef](#)]
23. MacDonald, M.; Zhitomirsky, I. Capacitive Properties of Ferrimagnetic NiFe<sub>2</sub>O<sub>4</sub>-Conductive Polypyrrole Nanocomposites. *J. Compos. Sci.* **2024**, *8*, 51. [[CrossRef](#)]

24. Devendra, B.K.; Praveen, B.; Tripathi, V.; Nagaraju, G.; Prasanna, B.; Shashank, M. Development of rhodium coatings by electrodeposition for photocatalytic dye degradation. *Vacuum* **2022**, *205*, 111460. [[CrossRef](#)]
25. Pandiyarajan, S.; Ganesan, M.; Liao, A.-H.; Manickaraj, S.S.M.; Huang, S.-T.; Chuang, H.-C. Ultrasonic-assisted supercritical-CO<sub>2</sub> electrodeposition of Zn-Co film for high-performance corrosion inhibition: A greener approach. *Ultrason. Sonochem.* **2021**, *72*, 105463. [[CrossRef](#)]
26. Hajnorouzi, A.; Modaresi, N. Direct sono electrochemical method for synthesizing Fe<sub>3</sub>O<sub>4</sub> nanoparticles. *J. Magn. Magn. Mater.* **2020**, *505*, 166732. [[CrossRef](#)]
27. Zhang, H.; Wang, J.; Chen, S.; Wang, H.; He, Y.; Ma, C. Ni-SiC composite coatings with improved wear and corrosion resistance synthesized via ultrasonic electrodeposition. *Ceram. Int.* **2021**, *47*, 9437–9446. [[CrossRef](#)]
28. Mladenović, I.; Lamovec, J.; Radović, D.V.; Radojević, V.; Nikolić, N.D. Influence of intensity of ultrasound on morphology and hardness of copper coatings obtained by electrodeposition. *J. Electrochem. Sci. Eng.* **2022**, *12*, 603–615. [[CrossRef](#)]
29. Costa, J.M.; de Almeida Neto, A.F. Ultrasound-assisted electrodeposition and synthesis of alloys and composite materials: A review. *Ultrason. Sonochem.* **2020**, *68*, 105193. [[CrossRef](#)]
30. Duan, B.; Zhu, Z.; Sun, C.; Zhou, J.; Walsh, A. Preparing copper catalyst by ultrasound-assisted chemical precipitation method. *Ultrason. Sonochem.* **2020**, *64*, 105013.
31. Bengoa, L.N.; Ispas, A.; Bengoa, J.F.; Bund, A.; Egli, W.A. Ultrasound assisted electrodeposition of Cu-SiO<sub>2</sub> composite coatings: Effect of particle surface chemistry. *J. Electrochem. Soc.* **2019**, *166*, D244. [[CrossRef](#)]
32. Zhang, H.; Wang, J.; Duan, H.; Ren, J.; Zhao, H.; Zhou, C.; Qi, J. Mn<sup>3+</sup> partially substituting the Ni<sub>3+</sub> of NiCo<sub>2</sub>O<sub>4</sub> enhance the charge transfer kinetics and reaction activity for hybrid supercapacitor. *Appl. Surf. Sci.* **2022**, *597*, 153617. [[CrossRef](#)]
33. Ádám, A.A.; Szabados, M.; Varga, G.; Papp, B.; Musza, K.; Kónya, Z.; Kukovecz, A.; Sipos, P.; Pálkó, I. Ultrasound-assisted hydrazine reduction method for the preparation of nickel nanoparticles, physicochemical characterization and catalytic application in Suzuki-Miyaura cross-coupling reaction. *Nanomaterials* **2020**, *10*, 632. [[CrossRef](#)] [[PubMed](#)]
34. Li, B.; Mei, T.; Chu, H.; Wang, J.; Du, S.; Miao, Y.; Zhang, W. Ultrasonic-assisted electrodeposition of Ni/diamond composite coatings and its structure and electrochemical properties. *Ultrason. Sonochem.* **2021**, *73*, 105475. [[CrossRef](#)] [[PubMed](#)]
35. Xu, S.; Wu, Q.; Wu, J.; Kou, H.; Zhu, Y.; Ning, C.; Dai, K. Ultrasound-assisted synthesis of nanocrystallized silicocarnotite biomaterial with improved sinterability and osteogenic activity. *J. Mater. Chem. B* **2020**, *8*, 3092–3103. [[CrossRef](#)] [[PubMed](#)]
36. Min, J.W.; Yim, C.J.; Im, W.B. Preparation and electrochemical characterization of flower-like Li<sub>1.2</sub>Ni<sub>0.17</sub>Co<sub>0.17</sub>Mn<sub>0.5</sub>O<sub>2</sub> microstructure cathode by electrospinning. *Ceram. Int.* **2014**, *40*, 2029–2034. [[CrossRef](#)]
37. Ding, Q.; Dou, Y.; Liao, Y.; Huang, S.; Wang, R.; Min, W.; Chen, X.; Wu, C.; Yuan, D.; Liu, H.K.; et al. Oxygen Vacancy-Rich Ultrathin Co<sub>3</sub>O<sub>4</sub> Nanosheets as Nanofillers in Solid-Polymer Electrolyte for High-Performance Lithium Metal Batteries. *Catalysts* **2023**, *13*, 711. [[CrossRef](#)]
38. Liu, G.; Liu, Y.; Luo, J.; Wang, Y.; He, J.; Shi, X.; Nie, Z.; Lu, X. Surface Corrosion Engineering Endows Mn-Doped NiCo<sub>2</sub>O<sub>4</sub> Nanosheets with High Capacity and Long Life for Alkaline Zn-Based Batteries. *ACS Appl. Energy Mater.* **2024**, *7*, 2234–2240. [[CrossRef](#)]
39. Xing, Z.; Ju, Z.; Zhao, Y.; Wan, J.; Zhu, Y.; Qiang, Y.; Qian, Y. One-pot hydrothermal synthesis of Nitrogen-doped graphene as high-performance anode materials for lithium ion batteries. *Sci. Rep.* **2016**, *6*, 26146. [[CrossRef](#)]
40. Dillinger, B.; Suchicital, C.; Clark, D. The effects of ultrasonic cavitation on the dissolution of lithium disilicate glass. *Sci. Rep.* **2022**, *12*, 20398. [[CrossRef](#)]
41. Salam, M.A.; Imdadulhaq, E.S.; Al-Romaizan, A.N.; Saleh, T.S.; Mostafa, M.M.M. Ultrasound-Assisted 1, 3-Dipolar Cycloadditions Reaction Utilizing Ni-Mg-Fe LDH: A Green and Sustainable Perspective. *Catalysts* **2023**, *13*, 650. [[CrossRef](#)]
42. Tsai, Y.-C.; Yang, W.-D.; Lee, K.-C.; Huang, C.-M. An effective electrodeposition mode for porous MnO<sub>2</sub>/Ni foam composite for asymmetric supercapacitors. *Materials* **2016**, *9*, 246. [[CrossRef](#)] [[PubMed](#)]
43. Vazhayil, A.; Thomas, J.; Thomas, T.; Hasan, I.; Thomas, N. Mn-substituted NiCo<sub>2</sub>O<sub>4</sub>/rGO composite electrode for supercapacitors and their electrochemical performance boost by redox additive in alkaline electrolyte. *J. Energy Storage* **2024**, *84*, 110789.
44. Raman, V.; Mohan, N.V.; Balakrishnan, B.; Rajmohan, R.; Rajangam, V.; Selvaraj, A.; Kim, H.J. Porous shiitake mushroom carbon composite with NiCo<sub>2</sub>O<sub>4</sub> nanorod electrochemical characteristics for efficient supercapacitor applications. *Ionics* **2020**, *26*, 345–354. [[CrossRef](#)]

**Disclaimer/Publisher’s Note:** The statements, opinions and data contained in all publications are solely those of the individual author(s) and contributor(s) and not of MDPI and/or the editor(s). MDPI and/or the editor(s) disclaim responsibility for any injury to people or property resulting from any ideas, methods, instructions or products referred to in the content.